

Numerical study of the flow structure and heat transfer in rotating cavity with and without jet*

K. KIELCZEWSKI, E. TULISZKA-SZNITKO

*Institute of Thermal Engineering
Poznań University of Technology
ul. Piotrowo 3
60-965, Poznań, Poland
e-mails: ewa.tuliszka-sznitko@put.poznan.pl
kamil.kielczewski@doctorate.put.poznan.pl*

IN THE PAPER WE INVESTIGATE the flow with heat transfer in the rotating cavity of different geometrical parameters and different Reynolds numbers. We focus on the near-wall characteristics and compare our results with the experimental and numerical data published in literature as well as with the theoretical results. We also present the preliminary results obtained for rotor/rotor configurations with the axial annular jet. Computations are performed using pseudo-spectral methods. Parallelization of the DNS code allows us to perform computations on the meshes with up to 35 million collocation points.

Key words: rotating flows, turbulent flow, heat transfer, pseudo spectral methods.

Copyright © 2013 by IPPT PAN

1. Introduction

THE PROBLEM OF LAMINAR-TURBULENT TRANSITION and turbulence in the near-wall sublayer is far from being solved, both in terms of understanding of physics and in terms of obtaining engineering accuracy for different devices in which turbulent flows play an important role (fluid flow machines, aircraft and automobile industries). The engineering and economic aspects prompt the ongoing research aimed at transferring new ideas from theory to industry. The near-wall sublayer is presently mostly modelled based on the existing knowledge of simple 2D models (zero-pressure gradient boundary layers and plane channel flow). It is believed that the understanding of the structure of coherent eddies in transitional and turbulent areas in simple model flows helps to understand more complex wall flows. This knowledge can contribute to wall turbulence control and to the development of scaling ideas. Additionally, the knowledge of turbulent flow structures, their origins, their role in creating stress and transporting energy can help to understand the nature of the turbulence. The understanding

*The paper was presented at XX KKMP conference, Gliwice, 17–20 September, 2012.

of the fundamental physical characteristics of the near-wall flows is the main area of our interest. We use the strong 3D non-isothermal rotor/stator and rotor/rotor model flows (a few cases with axial annular jet are also investigated) to study numerically the structure of the near-wall sublayer. These simple model flows with heat transfer contain Reynolds stresses which transport mean momentum and they also produce and dissipate turbulent kinetic energy. Rotor/rotor and rotor/stator flows are the simplest possible wall flows which exhibit most of the phenomena that are needed to understand strong 3D transitional and turbulent flows in more general flow cases – these models are particularly suitable for engineers dealing with gas turbines and axial compressors.

The flow in rotor/stator cavity was investigated experimentally and numerically among others by RANDRIAMAMPINANINA *et al.* [1], SERRE and PULICANI [2], SERRE, TULISZKA-SZNITKO, BONTOUX [3], LYGREN and ANDERSON [4], PONCET and SCHIESTEL [5], SEVERAC and SERRE [6], RANDRIAMAMPINANINA *et al.* [7], PELLE and HARMAND [8], TULISZKA-SZNITKO *et al.* [9, 10]. PELLE and HARMAND [8] performed measurements over the rotor (in the rotor/stator configuration) using a technique based on infrared thermography. TULISZKA-SZNITKO *et al.* [9, 10] performed computations of the non-isothermal flow in the rotor/stator cavity, delivering distributions of the local Nusselt numbers along the stator and rotor for different configurations and Reynolds numbers. The axial throughflow (rotor/stator configuration) with heat transfer was numerically investigated in [5] using RANS method.

The main motivation of our work is to investigate the characteristics of the near-wall flows. We present characteristics obtained in the stator boundary layer and preliminary results obtained in the heated rotor boundary layer under impingement of cold annular jet. Direct numerical simulations (DNS) of these flow cases require refined meshes with a large number of collocation points. To meet this requirement we apply the OpenMP technology to the code described in [9, 10]. Computations for the high aspect ratio $L = (R_1 - R_0)/H$ and large Reynolds numbers $Re = R_1^2 \Omega / \nu$ (presented in this paper) were performed with up to 35 million collocation points. These results are complementary to the results obtained for $L = 5-35$ with up to 10 million collocation points and published in [10]. We compare the present results with the experimental data of ELKINS and EATON [11] and the numerical results of KASAGI [12] and WU and KASAGI [13, 14].

Additionally, in the frame of this paper we implement the spectral vanishing viscosity method (SVV) to the parallelized DNS code for non-isothermal flow in rotating cavity. The SVV method was previously used for the investigation of the isothermal flow in rotor/stator cavity by SEVERAC and SERRE [6]. The main purpose of SVV implementation is to provide a stable scheme for solving Navier–Stokes equations, which simultaneously preserves spectral accuracy

(the exponential rate of convergence, PASQUETTI and XU [15]). This method is suitable for the investigation of rotor/stator and rotor/rotor flow cases where laminar, transitional and fully turbulent areas coexist. In the paper we extend the SVV method [6] to non-isothermal flow and perform computations for the high Reynolds numbers in the rotor/stator cavity with heat transfer. The SVV is also used for preliminary investigations of the flow cases with annular jet. To check the exponential rate of convergence we use the benchmark published in [6].

The mathematical and geometrical models are described in Section 2. The numerical method is presented in Section 3. In Section 4 some results obtained for aspect ratio $L = 5$, curvature parameter $Rm = (R_1 + R_0)/(R_1 - R_0) = 1.8$, $Re = 400\,000\text{--}700\,000$ are presented to demonstrate the effectiveness of the SVV method. The near-wall characteristics and the comparison with the wall asymptotes are shown in Section 5. In Section 6 the preliminary results obtained for rotor/rotor cavity with the annular axial jet are discussed; the attention is focused on the local Nusselt number distributions and their correlations with the flow structure. Summary and conclusions are given in Section 7.

2. Mathematical and geometrical models

In the paper we investigate the non-isothermal flow in the cavity between rotor and stator, and between rotor and rotor of the inner and outer radius R_0 and R_1 , respectively (Fig. 1). The inter-disks spacing is denoted by H . The rotor rotates at uniform angular velocity $\Omega = \Omega \mathbf{e}_z$, where \mathbf{e}_z is the unit vector on the z axis. The flow is described by the Navier–Stokes, continuity and energy equations written in a cylindrical coordinate system (R, φ, Z) . Equations are written with respect to rotating frame of reference. The Boussinesq approximation is used to take into account the buoyancy effects induced by the involved body forces.

The dimensionless axial and radial coordinates are: $z = Z/(H/2)$, $z \in [-1, 1]$, $r = (2R - (R_1 + R_0))/(R_1 - R_0)$, $r \in [-1, 1]$. The velocity components and time

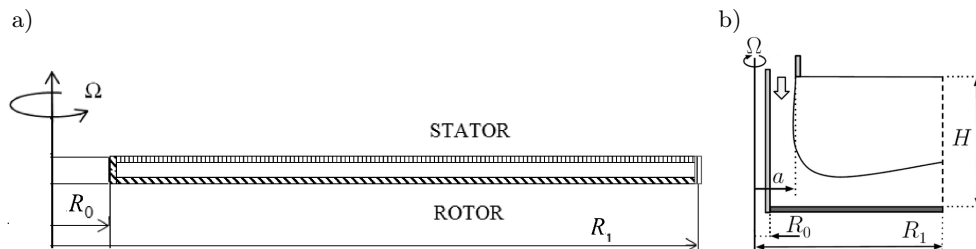


FIG. 1. Schematic pictures of: a) numerical domains of rotor/stator cavity, b) rotor/rotor configuration with axial annular jet.

are normalized by ΩR_1 and Ω^{-1} , respectively. The dimensionless components of the velocity vector in radial, azimuthal and axial directions are denoted by $u = U/\Omega R_1$, $v = V/\Omega R_1$, $w = W/\Omega R_1$. The dimensionless temperature is defined in the following way: $\Theta = (T - T_1)/(T_2 - T_1)$, where T_1 is the temperature of the upper disk and the inner cylinder, and T_2 is the temperature of the bottom heated rotating disk and the outer cylinder (rotor/stator configuration). In the rotor/rotor flow case only the bottom disk is heated. The flow is governed by the following dimensionless parameters: aspect ratio $L = (R_1 - R_0)/H$, curvature parameter $Rm = (R_1 + R_0)/(R_1 - R_0)$, the rotational Reynolds number $Re = \Omega R_1^2/\nu$, Prandtl number $Pr = 0.71$ and the thermal Rossby number $B = \beta(T_2 - T_1)$ (where β is thermal expansion coefficient).

In the rotor/stator flow case the boundary conditions are as follows: the rotating bottom disk is attached to the inner cylinder and the stator is attached to the outer cylinder. The no-slip boundary conditions are used with respect to all rigid walls, so $u = w = 0$. For the azimuthal velocity component, the boundary conditions are $v = 0$ on the rotating disk and $v = -(Rm + r)/(Rm + 1)$ on the stator. The thermal boundary conditions are as follows:

$$\begin{aligned} \Theta &= 1 \text{ for } z = -1.0, -1.0 \leq r \leq 1.0 \text{ and for outer cylinder,} \\ \Theta &= 0 \text{ for } z = 1.0, -1.0 \leq r \leq 1.0 \text{ and for inner cylinder.} \end{aligned}$$

The thermal Rossby number equals $B = 0.1$ in all considered flow cases.

In our preliminary investigation with the axial annular jet we assume that the nozzle, axial velocity component profile is constant. In the outer cylinder we apply constant radial velocity component or the convective condition. On the impinging wall we apply a no-slip condition and the temperature is constant.

3. Numerical methods

The temporal approximation used in the paper is a projection scheme which is based on backward differentiation in time. In every iteration a pressure predictor is computed by solving the pressure equation with the pressure Neumann boundary condition. The Navie–Stokes, continuity and energy equations are approximated in time using a second-order semi-implicit scheme, which combines an implicit treatment of the diffusive term and an explicit Adams–Bashforth approximation for the non-linear convective terms. The predicted velocity field is then corrected so that the final velocity field satisfies the incompressibility constraint. The correction is performed by introducing a special correction parameter ϕ : $p^{n+1} = p^p + 3\phi/2\delta t$, where $n + 1$ and p depict present iteration and predictor, δt is the increment of time. All dependent variables (predictors of three velocity components, predictor of pressure, temperature and corrector; $\Psi = [u, v, w, p, \Theta, \phi]$) are obtained by solving Helmholtz equation which can be

written in the following form:

$$(3.1a) \quad \underbrace{\frac{1}{L^2} \frac{\partial^2 \Psi}{\partial r^2} + \frac{1}{L^2(\text{Rm} + r)} \frac{\partial \Psi}{\partial r} + \frac{1}{L^2(\text{Rm} + r)^2} \frac{\partial^2 \Psi}{\partial \varphi^2} + \frac{\partial^2 \Psi}{\partial z^2}}_{\Delta \Psi} - q\Psi = S,$$

where q is a constant or is a function of r , function S contains terms obtained in previous iterations and obtained in the predictor stage. Detailed description of the iteration process is given in [2] and [10]. The spatial approximation is based on a pseudo-spectral Chebyshev–Fourier–Galerkin collocation method: the approximations of the variables $\Psi = [u, v, w, p, \Theta, \phi]$ are given by the development into truncated series:

$$(3.1b) \quad \Psi(r, \varphi, z) = \sum_{k=-N^\varphi/2}^{N^\varphi/2-1} \sum_{n=0}^{N^r-1} \sum_{m=0}^{N^z-1} \hat{\Psi}_{nmk} T_n(r) T_m(z) e^{ik\varphi},$$

$$-1 \leq r, z \leq 1, 0 \leq \varphi \leq 2\pi,$$

where $T_n(r)$ and $T_m(z)$ are Chebyshev polynomials and N^r , N^φ and N^z are numbers of collocation points in radial, azimuthal and axial directions, respectively. In the radial and axial directions we use Chebyshev polynomials with the Gauss–Lobatto distributions to ensure high accuracy of the solution inside the very thin boundary layers at the disks.

In the SVV method an artificial viscous operator is added to Laplace operator to stabilize the computational process. This SVV operator is sufficiently large to suppress Gibbs oscillations and small enough not to affect the solution accuracy (TADMOR [17], KARAMANOS and KARNIADAKIS [18]). The one-dimensional SVV viscous operator [17] can be written in the following way:

$$(3.2a) \quad \tilde{\Delta}_N u_N \equiv \varepsilon_N \frac{\partial}{\partial x} \left(Q_N \frac{\partial u_N}{\partial x} \right).$$

After adding (3.2a) to the Laplace operator we have

$$(3.2b) \quad \nu \Delta^{SVV} u_N = \nu \Delta u_N + \varepsilon_N \frac{\partial}{\partial x} \left(Q_N \frac{\partial u_N}{\partial x} \right),$$

where N is the number of collocation points, u_N is a discrete approximation of velocity component u , ε_N is the viscosity amplitude ($\lim_{N \rightarrow \infty} \varepsilon_N = 0$) and Q_N is the spectral operator active only for high frequencies [6, 19]. The operator (3.2a) in Fourier space can be written in the following form:

$$(3.3a) \quad \varepsilon_N \frac{\partial}{\partial x} \left(Q_N \frac{\partial u_N}{\partial x} \right) = -\varepsilon_N \sum_{k_T \leq |k| \leq N/2} k^2 \hat{Q}_{N/2}(k) \hat{u}_k e^{ikx},$$

where N is the number of Fourier mode and k_T is the threshold mode above which operator (3.2a) is active. In Chebyshev space Q_N works in the following way:

$$(3.3b) \quad Q_N \left(\frac{\partial u_N}{\partial x} \right) = \sum_{k=k_T}^N \hat{Q}_N(k) \frac{\partial \hat{u}_N}{\partial x} T_k,$$

where T_k are Chebyshev polynomials and \hat{Q}_N is defined as follows:

$$(3.3c) \quad \hat{Q}_N(k) = \begin{cases} 0 & \text{for } 0 \leq |k| \leq k_T, \\ \exp \left[- \left(\frac{N - |k|}{k_T - |k|} \right)^2 \right] & \text{for } k_T < |k| \leq N. \end{cases}$$

The SVV modes are activated over threshold k_T which can be taken as $N/2$ whereas the viscous amplitude ε_N can be taken as $O(1/N)$. The extension of definition (3.2a) to the 3D flow cases is discussed in [6, 15, 16, 18]. After [6] we can write:

$$(3.4a) \quad \nu \Delta^{SVV} u_N \equiv \nu \Delta u_N + \nabla \cdot (\varepsilon_N Q_N \cdot (\nabla u_N)) = \nu (\nabla \cdot G_N \cdot \nabla) u_N,$$

where

$$(3.4b) \quad G_N = I + \frac{1}{\nu} \varepsilon_N Q_N$$

$$= \begin{bmatrix} 1 + \varepsilon_{N^r}^r Q_{N^r}^r / \nu & 0 & 0 \\ 0 & 1 + \varepsilon_{N^\varphi}^\varphi Q_{N^\varphi}^\varphi / \nu & 0 \\ 0 & 0 & 1 + \varepsilon_{N^z}^z Q_{N^z}^z / \nu \end{bmatrix} = \begin{bmatrix} G_{N^r}^r & 0 & 0 \\ 0 & G_{N^\varphi}^\varphi & 0 \\ 0 & 0 & G_{N^z}^z \end{bmatrix},$$

∇u_N is the velocity gradient tensor, $\varepsilon_{N^i}^i$ is a viscosity amplitude for i direction, $Q_{N^i}^i$ is a viscosity operator which is defined in spectral space by Eq. (3.3c). In the next step the modified Laplace operator (3.4a) is introduced to our DNS algorithm. In DNS algorithm all dependent variables are obtained by solving Helmholtz equation (3.1a) using (3.1b) approximation. In the first step equation (3.1a) is expanded into Fourier series:

$$(3.5) \quad \frac{1}{L^2} \frac{\partial^2 \hat{\Psi}_k}{\partial r^2} + \frac{1}{L^2(\text{Rm} + r)} \frac{\partial \hat{\Psi}_k}{\partial r} + \frac{\partial^2 \hat{\Psi}_k}{\partial z^2} - \left[q + \frac{k^2}{L^2(\text{Rm} + r)^2} \right] \hat{\Psi}_k = \hat{S}_k,$$

$$k \in [-N^\varphi/2, \dots, N^\varphi/2 - 1].$$

After spatial discretization in radial and axial direction we can write

$$(3.6) \quad A\Psi + \Psi B = S, \quad \Psi = \hat{\Psi}_{ijk} = \hat{\Psi}_k(r_i, z_j), \quad S = \hat{S}_{ijk} = \hat{S}_k(r_i, z_j),$$

$$-1 \leq r_i, z_j \leq 1,$$

where

$$(3.7) \quad \begin{aligned} A_{ij} &= \frac{1}{L^2} Dr_{ij}^{(2)} + \frac{1}{L^2(\text{Rm} + r_i)} Dr_{ij}^{(1)} - \left[q_i + \frac{k^2}{L^2(\text{Rm} + r_i)^2} \right] \delta_{ij}, \\ B_{ij} &= Dz_{ji}^{(2)}. \end{aligned}$$

$Dr_{ij}^{(1)}$, $Dr_{ij}^{(2)}$, $Dz_{ij}^{(2)}$ are differentiating matrices. In the SVV method, the Laplace operator in Eq. (3.1a):

$$(3.8) \quad \Delta = \frac{1}{L^2} \frac{\partial^2}{\partial r^2} + \frac{1}{L^2(\text{Rm} + r)} \frac{\partial}{\partial r} + \frac{1}{L^2(\text{Rm} + r)^2} \frac{\partial^2}{\partial \varphi^2} + \frac{\partial^2}{\partial z^2}$$

is modified and takes the following form:

$$(3.9) \quad \begin{aligned} \Delta^{SVV} &\equiv \frac{1}{L^2} \frac{\partial}{\partial r} G_{N^r}^r \frac{\partial}{\partial r} + \frac{1}{L^2(\text{Rm} + r)} G_{N^r}^r \frac{\partial}{\partial r} \\ &\quad + \frac{1}{L^2(\text{Rm} + r)^2} \frac{\partial}{\partial \varphi} G_{N^\varphi}^\varphi \frac{\partial}{\partial \varphi} + \frac{\partial}{\partial z} G_{N^z}^z \frac{\partial}{\partial z}. \end{aligned}$$

After expanding (3.9) in Fourier series and with Eq. (3.3a) we obtain

$$(3.10) \quad \begin{aligned} \Delta_k^{SVV} &= \frac{1}{L^2} \frac{\partial}{\partial r} G_{N^r}^r \frac{\partial}{\partial r} + \frac{1}{L^2(\text{Rm} + r)} G_{N^r}^r \frac{\partial}{\partial r} \\ &\quad - \frac{k^2}{L^2(\text{Rm} + r)^2} \hat{G}_{N^\varphi}^\varphi(k) + \frac{\partial}{\partial z} G_{N^z}^z \frac{\partial}{\partial z}. \end{aligned}$$

Matrices A_{ij} and B_{ij} can be written in the following form:

$$(3.11) \quad \begin{aligned} A_{ij} &= \frac{1}{L^2} Dr_{ij}^{(2)SVV} + \frac{1}{L^2(\text{Rm} + r)} Dr_{ij}^{(1)SVV} \\ &\quad - \left(q_i + \frac{k^2}{L^2(\text{Rm} + r)^2} \left(1 + \frac{\varepsilon_{N^\varphi}^\varphi}{\nu} \hat{Q}_{N^\varphi/2}^\varphi(k) \right) \right) \delta_{ij}, \\ B_{ij} &= Dz_{ji}^{(1)SVV}. \end{aligned}$$

In Eqs. (3.11) differentiating matrices $Dr_{ij}^{(1)SVV}$ and $Dr_{ij}^{(2)SVV}$ are defined in the following way:

$$(3.12) \quad \begin{aligned} [Dr_{ij}^{(2)SVV}] &= Dr^{(2)SVV} = Dr^{(1)} \cdot Dr^{(1)SVV}, \\ [Dr_{ij}^{(1)SVV}] &= Dr^{(1)SVV} = \left(I + \frac{1}{\nu} \varepsilon_{N^r}^r H^r \right) Dr^{(1)}. \end{aligned}$$

The matrix $Dz_{ij}^{(1)SVV}$ is defined in a similar way. H^r is Chebyshev high-pass filter [20] that is defined as follows (in z direction we obtain similar formulas):

$$(3.13) \quad H_{ij}^r = \frac{2}{N^r c_j} \sum_{n=0}^{N^r-1} \frac{1}{c_n} \hat{Q}_{N^r}^r(n) T_n(r_i) T_n(r_j),$$

where $c_j = \begin{cases} 2 & \text{for } j \in (0, N^r), \\ 1 & \text{for } j \in (1, \dots, N^r - 1), \end{cases}$

$$T_n(r_j) = \cos(n\pi(j)/N^r).$$

In order to verify the exponential convergence of the SVV method we use the benchmark described in [6]: the steady flow solution in cavity with $L = 5$, $\text{Rm} = 5$, $\text{Re} = 500$ has the following analytical solution:

$$(3.14) \quad \begin{aligned} u_a &= \frac{2}{L(r + \text{Rm})} z^2 \tanh(1 - z^3) \sin(\varphi) \cos(2\varphi), \\ v_a &= 5 \cdot 10^{-2} (1 + 2 \ln(L(r + \text{Rm}))) z^2 \tanh(1 - z^3), \\ w_a &= 2 \cdot 10^{-1} \sin^2(L(r + \text{Rm})) \frac{1 + \sin(\varphi)}{2 + \cos(\varphi)}, \\ p_a &= 10^{-1} \tanh[1 - L^2(r + \text{Rm})^2] z^2 [\sin(\varphi) + \cos(2\varphi)]^2. \end{aligned}$$

Benchmark requires obtaining the function for mass force F from Navier–Stokes equations (what we did using the MAXIMA symbolic calculation tool). Then the disturbed flow field (3.14) [6] was used as an initial condition in our code. In our solver we took into account the mass force F . The boundary conditions were directly taken from (3.14). We performed computations for the following parameters: $\varepsilon = 1/N$, $\delta t = 0.01$, $N^\varphi = N^z = 57$ and for different numbers of collocation points in radial direction. Our computations confirm the exponential convergence of the SVV method for $N^r \geq 100$. The implemented SVV method turned out to be a very effective tool which allowed us to perform computations for high Reynolds numbers, even using mesh with a small number of collocation points ($N^r = 165$, $N^\varphi = 140$, $N^z = 61$).

4. SVV computations: rotor/stator case flow

To show the effectiveness of the SVV method, computations have been performed for rotor/stator configuration of $L = 5$, $\text{Rm} = 1.8$ on the mesh ($165 \times 140 \times 61$) with the use of the threshold value $N/2$ and $\varepsilon_N = 1/N$. At the beginning of our investigations we compare our SVV results with the DNS results obtained for transitional and weakly turbulent flow cases ($\text{Re} = 100\,000$, $200\,000$) and we obtain an agreement between these results. Then we perform computations for higher Re to compare our results with those obtained exper-

imentally in [6] for the isothermal flow in rotor/stator cavity of aspect ratio $L = 5$, $Rm = 1.8$, $Re = 400\,000$ (the outer stationary cylinder attached to the stator and the inner rotating cylinder attached to the rotor). All statistical quantities are averaged in time and in the azimuthal direction. Figure 2a presents the axial profile of the radial velocity component obtained in the middle section of cavity (velocity is normalized by the local velocity of the rotor as in [6] to make the direct comparison possible). We observe an agreement of our results with [6] data in spite of the fact that experimental investigations have been performed for the isothermal condition. We observe that the axial profiles consist of the boundary layer on the stator and on the rotor, and of the inviscid core between them (this type of flow is called the Batchelor flow, [4, 10]). All flow cases ($L = 5-45$) considered in the paper are of the Batchelor type; however, with increasing L the inviscid core is gradually shrinking. The axial profiles of mean azimuthal velocity component normalized by the total friction velocity $U_\sigma = [\nu^2((dU/dz)^2 + (dV/dz)^2)]^{0.25}$ in function of the axial coordinate with wall scaling $z^+ = ZU_\sigma/\nu$ are presented in Fig. 2b. The obtained profiles agree with the traditional wall law $v^+ = \ln(z^+)/0.41 + 5.5$ (statistics are gathered during 1–2 global time units, i.e., in terms of Ω^{-1}) and also with Kasagi’s [12] numerical results obtained for the rotating channel flow.

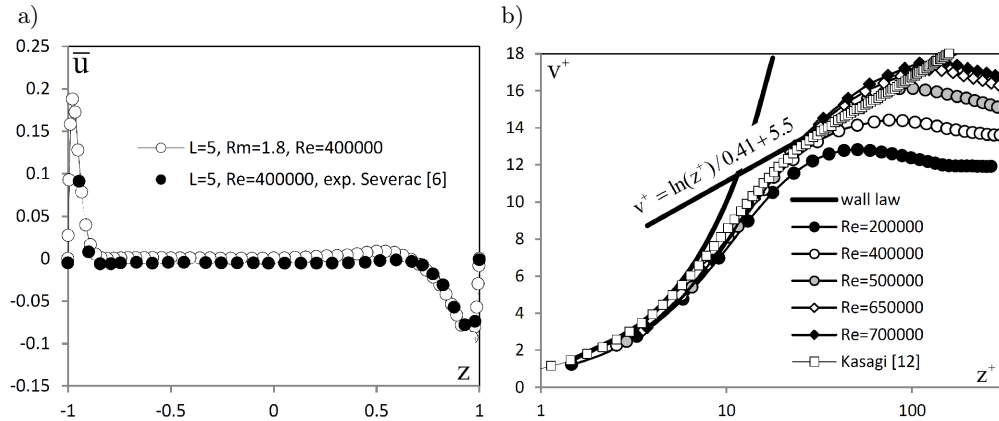


FIG. 2. a) The axial profiles of the radial velocity component obtained for $Re = 400\,000$ (velocity normalized by the local velocity of the rotor). Comparison with the experimental data [6]. b) Dimensionless azimuthal velocity profiles in function of axial coordinate in wall scaling obtained for different Reynolds numbers; comparison with the wall law. Comparison with Kasagi’s numerical results [12]. Middle section of cavity: $L = 5$, $Rm = 1.8$, $B = 0.1$, $Re = 400\,000$. SVV computations.

The distribution of the r.m.s. radial Reynolds stress tensor component $\overline{u'u'}^{0.5}$ obtained for $Re = 400\,000$ in the middle section of cavity is shown in Fig. 3a and compared with the experimental results published in [6]. Again, we observe

an agreement of our results with the experimental data in [6]. For the boundary conditions described in Section 2 the flow is pumped outward along the heated bottom disk (rotor). Then the fluid is lifted up along the heated stationary outer cylinder and recirculates along the cooled stator. Turbulence is concentrated in the stator boundary with the maximum at the junction between the outside cylinder and stator. The structures of the flows in the rotor and stator boundary layers are presented in Fig. 3b (iso-lines of the axial velocity component). In the stator boundary layer (Fig. 3b) we observe thin axisymmetrical structures typical of turbulent flows, whereas in the rotor boundary layer, positive spiral vortices are visible. The obtained flow structure is similar to this presented in [6]. We can conclude that the SVV correctly describes the structure of turbulent flows.

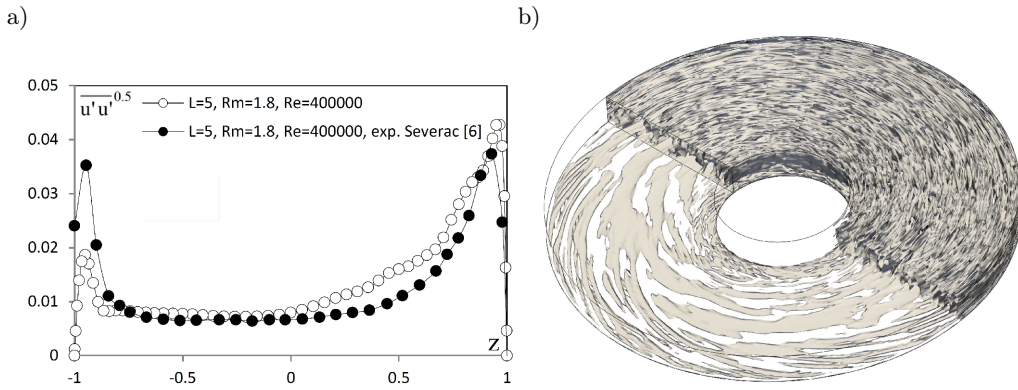


FIG. 3. a) The axial profile of square root of the radial Reynolds stress tensor component (normalized by the local velocity of the rotor). Middle section of the cavity. Comparison with the experimental data [6]. b) The iso-lines of axial velocity component obtained near the stator and rotor for $Re = 400\,000$, $L = 5$, $Rm = 1.8$ and, $B = 0.1$. SVV computations.

5. Near-wall structure of the flow

The parallelization of the DNS code (OpenMP technology) has allowed us to perform computations using a large number of collocation points which is particularly important in the near-wall area. Additionally, the use of the SVV method has allowed us to perform computations for high Reynolds numbers. The DNS/SVV of turbulent flow offers a wealth of information which cannot be obtained experimentally. Specifically, this study aims at comparing the axial distributions of the Reynolds stress tensor components and the turbulent heat flux components obtained in the near wall area with the wall asymptotes. The obtained data can be of interest for the researches dealing with the RANS method.

Figures 4–6 show the Reynolds stress tensor components normalized by the square of the friction velocity $\overline{V'V'}/U_\sigma^2$, $\overline{U'U'}/U_\sigma^2$, $\overline{W'W'}/U_\sigma^2$, $\overline{V'W'}/U_\sigma^2$ and the turbulent heat flux components $(\overline{T'T'})/T_\sigma T_\sigma$, $(\overline{T'V'})/T_\sigma U_\sigma$, $(\overline{T'W'})/T_\sigma U_\sigma$, $-\overline{(T'U')}/T_\sigma U_\sigma$ versus the axial coordinate in wall scaling z^+ obtained for different Re and L (middle section of cavity; $T_\sigma = \dot{q}_w/\rho c_p U_\sigma$ denotes friction temperature). The logarithmic scale is used on both axes. Figures 4–6 also show the slope of the wall asymptotes (black lines) which can be useful in predicting the fluid behavior in the near-wall area.

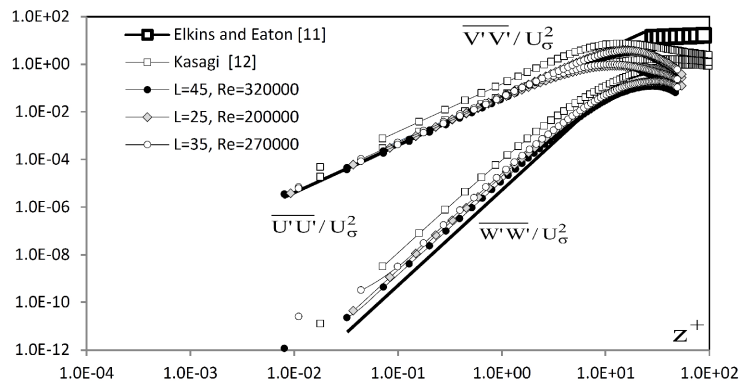


FIG. 4. The axial profiles of the three Reynolds stress tensor components $\overline{V'V'}/U_\sigma^2$, $\overline{U'U'}/U_\sigma^2$ and $\overline{W'W'}/U_\sigma^2$ versus the axial coordinate in wall scaling, obtained for different Re and L . $Rm = 1.8$, $B = 0.1$. Comparison with the numerical results obtained in [12–14], with the experimental data obtained in [11] and with the near wall asymptotes.

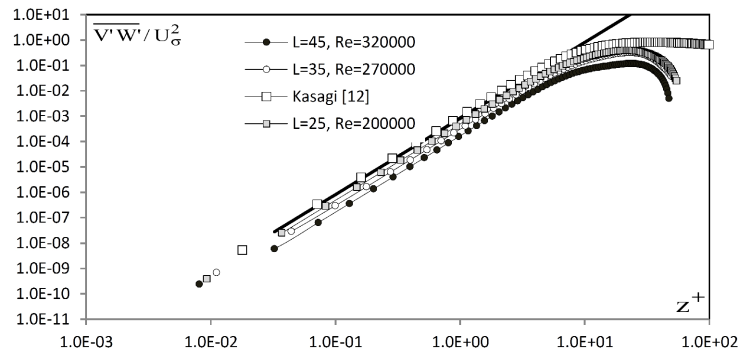


FIG. 5. The axial profiles of the Reynolds stress tensor component $\overline{V'W'}/U_\sigma^2$ versus the axial coordinate in wall scaling obtained for different Re and L . $Rm = 1.8$, $B = 0.1$. Comparison with the numerical results obtained in [12–14], and with the near wall asymptote.

In the near-wall area the changes of the fluid flow parameters in the axial direction are dominant. Following HANJALIĆ and LAUNDER [21] the velocity components, temperature and pressure fluctuations can be expanded into a Taylor

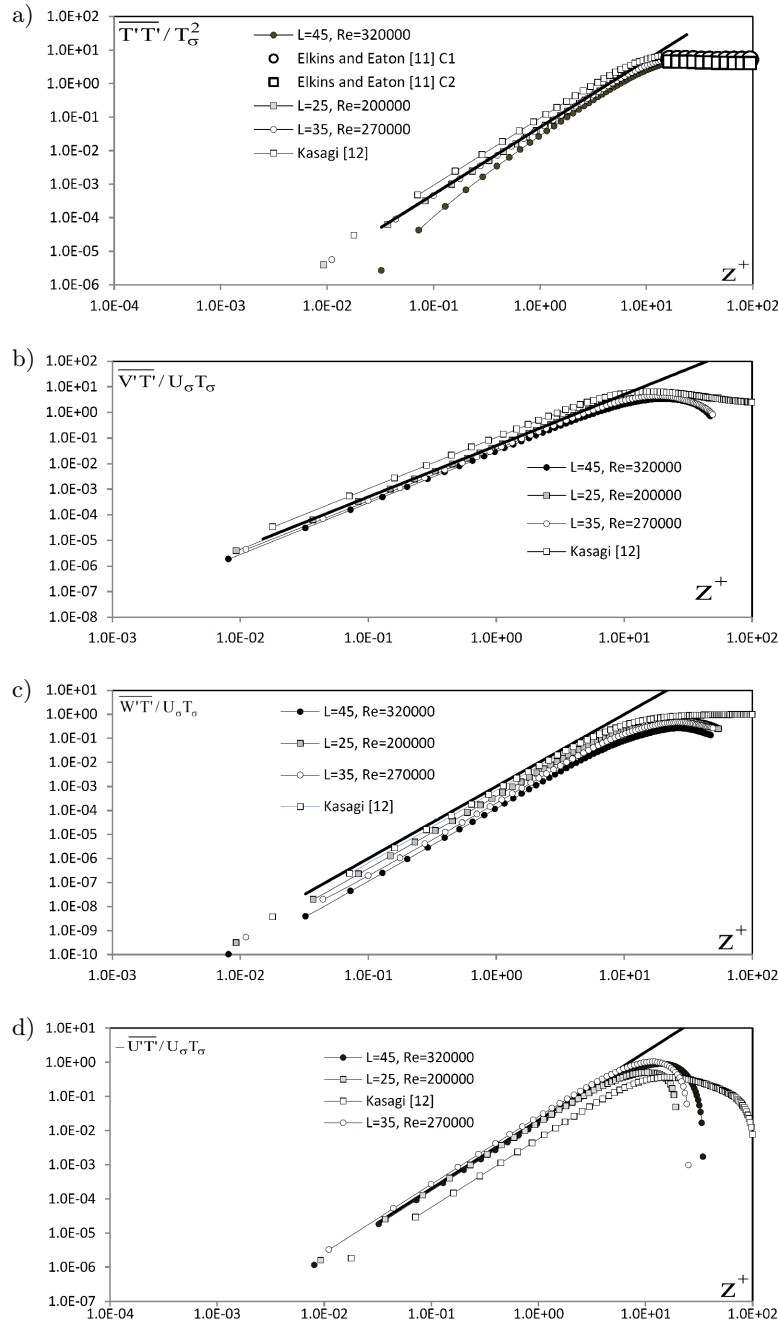


FIG. 6. a) The mean square temperature fluctuation profiles $\overline{T'T'}/T_\sigma^2$ versus the axial coordinate with wall scaling, b) $\overline{V'T'}/U_\sigma T_\sigma$, c) $\overline{W'T'}/U_\sigma T_\sigma$, d) $-\overline{U'T'}/U_\sigma T_\sigma$ obtained for $Rm = 1.8$, $B = 0.1$ and different L and Re . Comparison with the numerical results obtained in [12–14], with the experimental data obtained in [11] and with the near wall asymptotes.

series in the following way:

$$(5.1a) \quad \begin{cases} u'(\varphi, r, z, t) = a_u(\varphi, r, t) + b_u(\varphi, r, t)z + c_u(\varphi, r, t)z^2 + d_u(\varphi, r, t)z^3 \dots, \\ v'(\varphi, r, z, t) = a_v(\varphi, r, t) + b_v(\varphi, r, t)z + c_v(\varphi, r, t)z^2 + d_v(\varphi, r, t)z^3 \dots, \\ w'(\varphi, r, z, t) = a_w(\varphi, r, t) + b_w(\varphi, r, t)z + c_w(\varphi, r, t)z^2 + d_w(\varphi, r, t)z^3 \dots, \end{cases}$$

$$(5.1b) \quad \Theta'(\varphi, r, z, t) = a_T(\varphi, r, t) + b_T(\varphi, r, t)z + c_T(\varphi, r, t)z^2 + d_T(\varphi, r, t)z^3 \dots,$$

$$(5.1c) \quad p'(\varphi, r, z, t) = a_p(\varphi, r, t) + b_p(\varphi, r, t)z + c_p(\varphi, r, t)z^2 + d_p(\varphi, r, t)z^3 \dots$$

For the viscous flow cases with the no-slip condition velocity fluctuations at the wall equal zero ($u'_w = v'_w = w'_w = 0$) and consequently $a_u = a_v = a_w = 0$. Additionally, from the continuity equation written for velocity fluctuations (incompressible flow) we have at the wall: $(\partial w'/\partial z)_w = 0$ so that $b_w = 0$ in Eq. (5.1a). For isothermal condition at the wall there are no temperature fluctuations ($\Theta'_w = 0$) and consequently $a_T = 0$. After multiplication of appropriate fluctuations (described by Eqs. (5.1)) and averaging of the product in time we get the following estimations:

$$(5.2) \quad \begin{aligned} \overline{u'u'} \sim \overline{v'v'} \sim z^2, \quad \overline{w'w'} \sim z^4, \quad \overline{v'w'} \sim z^3, \quad \overline{u'w'} \sim z^3, \quad \overline{u'v'} \sim z^2, \\ \overline{u'\Theta'} \sim \overline{v'\Theta'} \sim z^2, \quad \overline{\Theta'\Theta'} \sim z^2, \quad \overline{w'\Theta'} \sim z^3. \end{aligned}$$

Our results obtained for very strong 3D boundary layers of the stator in rotor/stator configurations (Figs. 4–6) confirm the inferences (5.2). The results are compared with experimental data obtained in [11] for a single heated rotating disk and with numerical data in [12] obtained in fully developed channel flow with heat transfer and with streamwise system rotation. We can observe an agreement between all our results and the results in [12] with the near wall asymptotes up to $z^+ \approx 10$.

The Reynolds stress tensor components $\overline{v'w'}$, $\overline{u'w'}$ increase as $\sim z^3$ for the small distance from the wall (they are negligibly small in comparison to the viscous shear stresses). For larger distances from the wall $\overline{v'w'}$ and $\overline{u'w'}$ become the dominant contributors to the momentum transfer. The axial profiles of the total shear stress ($[(\nu\partial\bar{U}/\partial Z - \overline{U'W'})^2 + (\nu\partial\bar{V}/\partial Z - \overline{V'W'})^2]^{1/2}/\sigma_w$), the Reynolds shear stress ($[(\overline{U'W'})^2 + (\overline{V'W'})^2]^{1/2}/\sigma_w$) and the viscous shear stress are presented in Fig. 7 as a function of z^+ (σ_w denotes shear stress at the wall). We can see that the total shear stress is almost constant up to $z^+ \sim 3$ (thin layer in which viscous action is a dominant mechanism in momentum transfer). With increase of the distance from the wall we observe rapid decrease of the total shear stress (in this area the momentum is transferred mostly by the turbulent shear stresses). The Reynolds shear stress ($[(\overline{U'W'})^2 + (\overline{V'W'})^2]^{1/2}/\sigma_w$) reaches the maximum value at $z^+ \sim 17.3$ (Fig. 7).

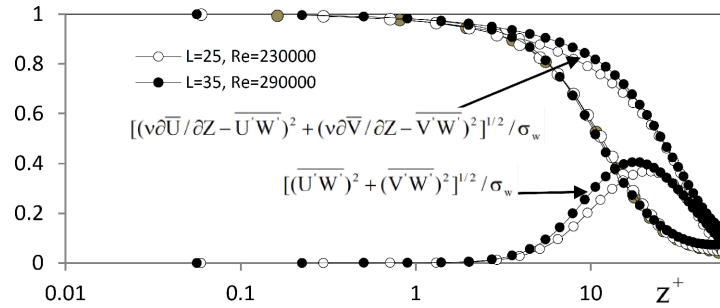


FIG. 7. The axial profiles of the total shear stress $[(\nu\partial\bar{U}/\partial Z - \overline{U'W'})^2 + (\nu\partial\bar{V}/\partial Z - \overline{V'W'})^2]^{1/2}/\sigma_w$, the Reynolds shear stress and the viscous shear stress in function of z^+ obtained for different L and Re . $Rm = 1.8$, $B = 0.1$. Middle section of cavity.

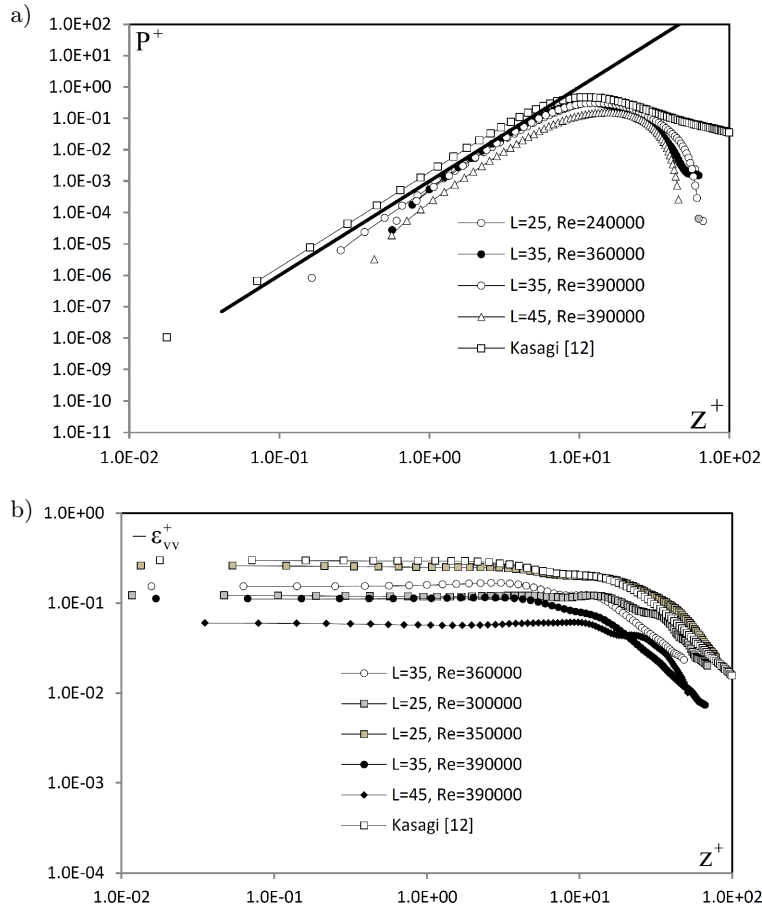


FIG. 8. a) The axial profiles of production rate P_{v^+} . b) The axial profiles of dissipation rate $-\epsilon_{vv}^+$. The middle section of cavity, $Re = 1.8$, $B = 0.1$. Comparison with the results obtained by KASAGI [12] and WU and Kasagi [13, 14].

In our investigations we also analyze the budget of transport equations (the transport equations in cylindrical co-ordinate system can be found in [22]). The Reynolds stress transport equation can be written in the symbolic form:

$$(5.3) \quad \frac{\partial \overline{U'_i U'_j}}{\partial t} = A_{ij} + R_{ij} + P_{ij} + TD_{ij} + PD_{ij} + PS_{ij} + VD_{ij} - \varepsilon_{ij}.$$

The physical significance of the particular terms are: A – advection, R – rotation, P – production, TD – turbulent diffusion, PD – pressure diffusion, PS – pressure strain, VD – viscous diffusion and ε – dissipation. The exemplary axial profiles of production P_{vv}^+ (Eq. (5.4a)) and dissipation ε_{vv}^+ (Eq. (5.4b)) in function of z^+ obtained for different L and Re are presented in Fig. 8. From Fig. 8a we estimate P_{vv}^+ that in the near-wall area is $P_{vv}^+ \approx 0.001(z^+)^3$. The stress dissipation rate ε_{vv}^+ in the near-wall area is constant – up to $z^+ \approx 10$. Most of the terms of the Reynolds stress budget can be estimated with approximations (5.1) [21]:

$$(5.4a) \quad P_{vv}^+ = \left(-2 \frac{1}{L} \frac{\partial \bar{v}}{\partial r} \overline{v' u'} - \frac{2}{L(Rm + r)} \left(\frac{\partial \bar{v}}{\partial \varphi} + \bar{u} \right) \overline{v' v'} - 2 \frac{\partial \bar{v}}{\partial z} \overline{w' v'} \right) \cdot Re \cdot \left[L(Rm + 1) \left(\left(\frac{\partial \bar{u}}{\partial z} \right)_w^2 + \left(\frac{\partial \bar{v}}{\partial z} \right)_w^2 \right) \right]^{-1},$$

$$(5.4b) \quad \varepsilon_{vv}^+ = \left(-2 \frac{1}{L^2} \overline{\left(\frac{\partial v'}{\partial r} \right) \left(\frac{\partial v'}{\partial r} \right)} - 2 \overline{\left(\left(\frac{\partial v'}{\partial \varphi} + u' \right) / L(Rm + r) \right)^2} - 2 \overline{\left(\frac{\partial v'}{\partial z} \right) \left(\frac{\partial v'}{\partial z} \right)} \right) \cdot \left(\left(\frac{\partial \bar{u}}{\partial z} \right)_w^2 + \left(\frac{\partial \bar{v}}{\partial z} \right)_w^2 \right)^{-1}.$$

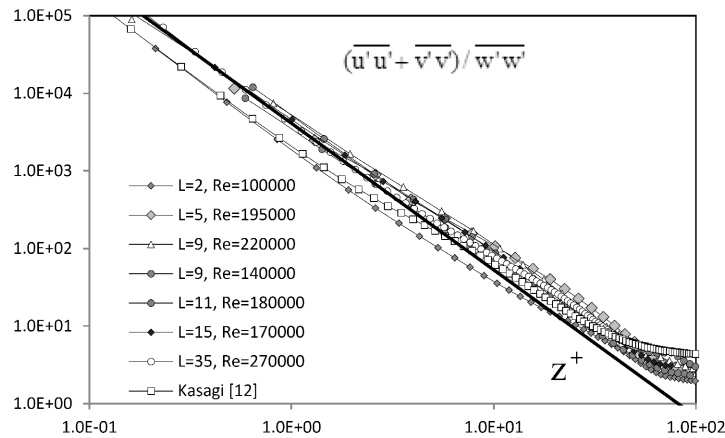


FIG. 9. The axial profiles of the structural parameter $(\overline{u'u' + v'v'}) / \overline{w'w'}$ versus axial coordinate in wall scaling z^+ . $Rm = 1.8$, $B = 0.1$, the stator boundary layer, middle section. Comparison with the results obtained in [12–14].

The structure of the near-wall flow can be also characterized by structural parameters which are very useful for modelling purposes, [11]. Figure 9 presents the distributions of the structural parameter $(\overline{u'u'} + \overline{v'v'})/\overline{w'w'}$ obtained for different L and Re . We observe that $(\overline{u'u'} + \overline{v'v'})/\overline{w'w'}$ varies as $\sim (z^+)^{-2}$ in the near-wall area (solid line). From Fig. 9 we can see that the values of $(\overline{u'u'} + \overline{v'v'})/\overline{w'w'}$ are very large near wall which implies that the vertical movement in this area is weak.

6. Local Nusselt number distributions along heated rotating disk under impinged jet

The flow between two rotating disks with a superimposed flow was investigated in many papers (OWEN and ROGERS [23], CRASPO DEL ARCO *et al.* [24], among others). Problem is of great interest for the internal aerodynamics of engines, particularly can be interesting for engineers dealing with turbomachinery air-cooling devices. However, it is also interesting from fundamental point of view. Craspo del Arco *et al.* [24] investigated numerically the spatio-temporal behavior of the flow in the rotor/rotor cavity with radial inflow and the radial outflow. They analyzed consecutive bifurcations in the Ekman boundary layer, which appeared with the increasing mass flow rates. In the present paper we performed preliminary computations of the flow with heat transfer between two rotating disks with the axial inflow and the radial outflow. We focused on the Nusselt number distributions near the axial annular impinging area and on its correlations with the flow structure.

The local Nusselt number is computed from the equation:

$$(6.1) \quad \text{Nu}_r = \frac{1}{(1 - \Theta_c)} \left(\frac{\partial \Theta}{\partial z} \right)_w L(\text{Rm} + r),$$

where $\Theta_c(r)$ denotes the dimensionless temperature in the core of cavity ($z = 0$), averaged in time and in the azimuthal direction. The distributions of the local Nusselt numbers along rotor and stator (rotor/stator cavity) obtained for different geometrical and physical parameters are analyzed in detail in [9, 10]. In the present paper we compare these results (Fig. 10) with the preliminary results obtained for the flow cases with annular axial jet impinging on the heated rotor using DNS and SVV (rotor/rotor cavity). Computations have been performed for very low Reynolds number. These preliminary results (obtained using the same mesh with Gauss-Lobatto collocation points which was previously used for rotor/stator cavity; $400 \times 400 \times 200$) allow us to estimate the correlations between the local Nusselt number distributions along disk and the resulting flow structures. However, this approach is very time consuming so that only some flow cases have been computed (in our computations we increase gradually the

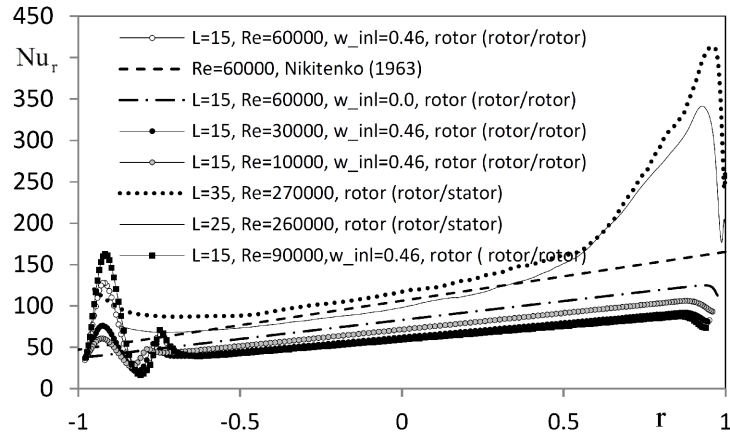


FIG. 10. Distributions of the local Nusselt numbers obtained along heated rotor.

axial velocity component at the inlet w_{inl} with very small increment). The dimensionless time step is $\delta t = 10^{-5}$. All computed flow cases with jet are laminar. The exemplary fluid flow structure and temperature field obtained for $L = 15$, $Rm = 1.8$, $Re = 90\,000$, $(r_a - r_{R_0}) = 0.02791$, $w_{\text{inl}} = 0.46$ are presented in Fig. 11 (only the inlet area is visible).

Investigation of spatio-temporal flow between two rotating discs with radial inflow and outflow, was investigated by some authors (among others [24]). Crespo del Arco *et al.* analyzed consecutive bifurcations which occur with the increasing mass flow rates. The authors concluded that dynamical behavior of the flow in rotor/rotor cavity results in instability of the entry flow. In present paper we analyzed laminar flow in rotor/stator cavity with axial inflow and radial outflow.

The radial profiles of the axial velocity components obtained for different axial sections are presented in Fig. 11c. From Fig. 11a we can see that the cold fluid enters the cavity through the upper disk and the axial annular jet impinges on the bottom heated rotating disk. As the cold fluid approaches the wall the axial velocity component vanishes and the fluid changes its direction. The fluid is pumped radially outward as a wall jet and then it is disgorged to flow radially inward. In this area a large vortex is observed which intensifies the redistribution of the hot and cold fluids.

In Fig. 10 we present the Nusselt number distributions obtained along heated rotor (rotor/stator configuration, $Re = 270\,000$, $L = 35$, $Rm = 1.8$ and $Re = 260\,000$, $L = 25$, $Re = 1.8$), results obtained along the heated rotor under impingement of cold jet (rotor/rotor configurations with annular impinging jet, different Re , $(r_a - r_{R_0}) = 0.02791$, $w_{\text{inl}} = 0.46$), results obtained along the heated rotor (rotor/rotor configurations without annular impinging jet, $Re = 60\,000$)

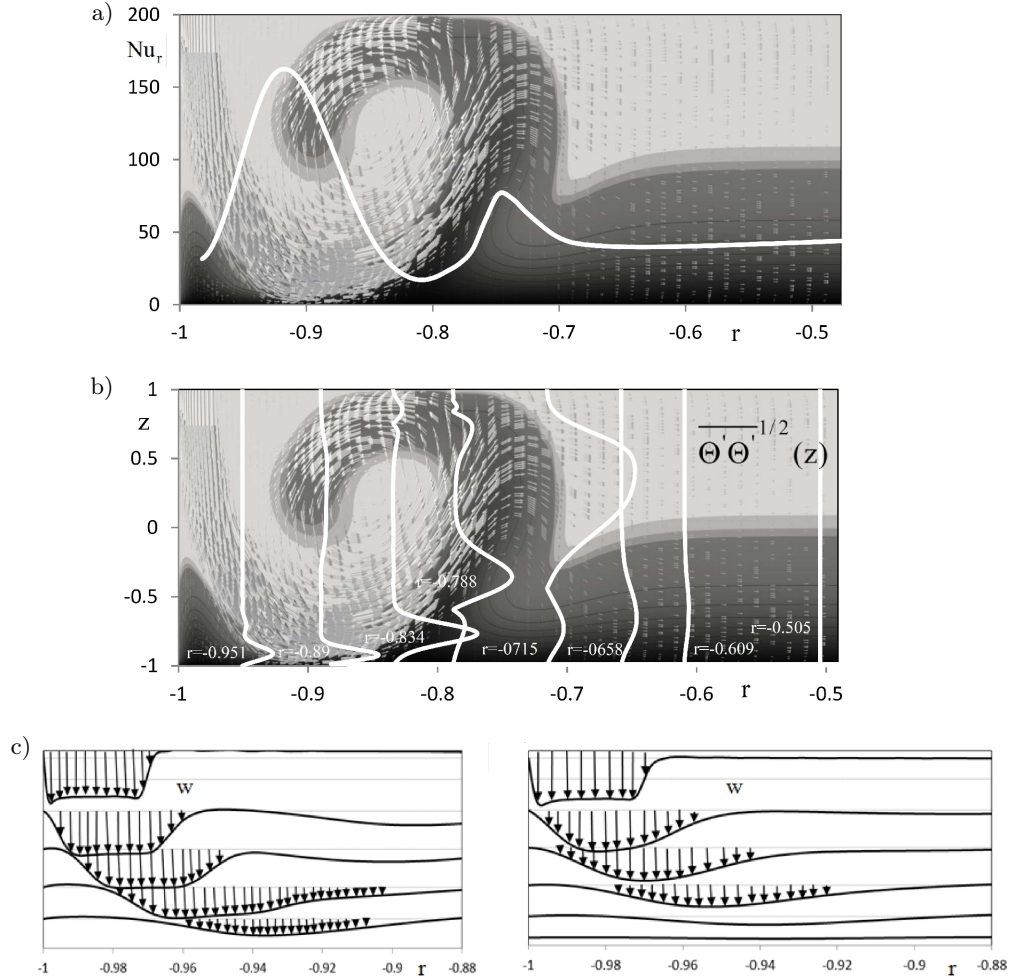


FIG. 11. a) The meridian fluid flow and temperature fields, the local Nusselt number distribution: $Re = 90\,000$, $L = 15$, $Rm = 1.8$, $(r_a - r_{R_0}) = 0.02791$. b) The meridian fluid flow and temperature fields, the axial profiles of the temperature fluctuations, $Re = 90\,000$, $L = 15$, $Rm = 1.8$, $(r_a - r_{R_0}) = 0.02791$. c) The radial profiles of the axial velocity components obtained for $Re = 90\,000$, $L = 15$, $Rm = 1.8$, $(r_a - r_{R_0}) = 0.02791$ (left) and $Re = 40\,000$, $L = 15$, $Rm = 3.0$, $(r_a - r_{R_0}) = 0.02791$ (right).

and results obtained from the experimental correlation formula proposed by NIKITENKO [25] for the heated rotating disk. The local Nusselt number varies linearly with the radius of the rotating disk in laminar flow $Nu_r \sim Re_r^{0.5}$ and in accordance with function $Nu_r \sim Re_r^{0.8}$ in turbulent flow ($Re_r = \Omega R^2 / \nu$). We can see from Fig. 10 that for flow cases with $L = 35$ and $L = 25$, Nu_r is a linear function of the radius in the range $-0.8 < r < 0.5$. In the area near the outer cylinder ($r \geq 0.5$) where the turbulence level is high we observe rapid increase

of the local Nusselt number (there is a change of the slope of the curves). Distributions obtained in [25] formula and obtained from DNS (rotor/rotor cavity without jet, $Re = 60\,000$, $L = 15$, $Rm = 1.8$) are linear along the whole rotor. In the flow cases with the axial laminar annular jet we observe rapid changes of the local Nusselt number near the impinging area; for larger radii we again observe the linear distribution of Nu_r .

Figure 11a shows correlation between the fluid flow structure and temperature structure, and the local Nusselt number distribution ($Re = 90\,000$). The maximum value of the Nusselt number is observed in the area where the bottom disk's boundary layer is the thinnest, then Nu_r decreases to the minimal value at $r \approx -0.8$. The second peak of the local Nusselt number occurs at $r \approx -0.75$. Outside of the impingement area the Nusselt number increases linearly with the radius. Figure 11b shows correlation between the fluid flow structure, temperature structure and the axial profiles of the temperature fluctuations $\overline{\theta'\theta'^{0.5}}$ obtained in the different radial sections of the cavity ($Re = 90\,000$). The maximum value of the axial $\overline{\theta'\theta'^{0.5}}$ profiles depends very strongly on the radius of the considered section (outside of the large vortex presented in Fig. 11 temperature fluctuations are negligibly small).

7. Summary and conclusions

In the paper we presented DNS/SVV computations of the flow with heat transfer in rotating cavity of different aspect ratio $L = 5-45$, $Rm = 1.8$ and different Reynolds numbers. We also presented a few preliminary solutions obtained for the rotor/rotor flow cases with the axial annular jet. The main purpose of the paper was to investigate the characteristics of the near-wall flows. To obtain this goal we parallelized existing DNS code and then implemented the spectral vanishing viscosity method (SVV) to stabilize the discretization scheme.

We verified the exponential convergence of the SVV by the benchmark described in [6]. The SVV method turned out to be a very efficient numerical tool which enabled us to perform computations for higher Re (even on meshes with the small number of collocation points). In Section 3 we compared our results obtained for the rotor/stator cavity of $L = 5$, $Rm = 1.8$, $B = 0.1$ and for $Re = 400\,000$ using the SVV method with the experimental results obtained in [6] for the same geometrical parameters and Reynolds number but for the isothermal condition. We found an agreement between the experimental and the numerical results. We also demonstrated that the stator boundary layer flows satisfy the traditional wall law (turbulence statistics were gathered for 1–2 global time units). In the frame of the present paper the SVV-Laplace operator Δ^{SVV} was only applied to the Navier–Stokes equation. In the near future we plan to ap-

ply Δ^{SVV} to the energy equation. This extension should lead to further increase of the scheme stability.

In studies of the flow with heat transfer in the rotor/stator cavity with higher L we used refined mesh with up to 35 million collocation points. The obtained results are complementary to those published in [10] where the solutions obtained using the meshes with up to 10 million collocation points were presented. The refined meshes enabled us to carefully investigate near-wall area (to the best knowledge of the authors such a detailed information cannot be obtained experimentally). All considered rotor/stator flow cases were of Batchelor type (the flow consists of two boundary layers separated by a rotating inviscid core); however, with increasing aspect ratio the inviscid core gradually disappears. We presented the axial distributions of the Reynolds stress tensor components, the turbulent heat flux components, the production and dissipation rates and selected structural parameters in function of the wall coordinate. Our results were compared with the experimental data from [11] obtained for the heated single rotating disk and with the numerical results of [12] obtained in a fully developed channel flow with heat transfer and with streamwise system rotation, and with the wall asymptotes. We observed an agreement between all results with the wall asymptotes up to $z^+ \approx 10$. These results can be useful for RANS modelers. The authors are also interested in comparison of their results (3D, SVV/DNS) with those obtained numerically using different RANS models (RSM, $k-\varepsilon$, [1]). Such a comparison could help to estimate the strengths and limitations of particular models.

We also presented the preliminary results (DNS/SVV) of the flow in rotor/rotor cavity with the axial annular jet impinging on the heated rotating disk. All considered flow cases were laminar. We focused on the correlations between the resulting large scale structures and the distributions of the local Nusselt number, and the distributions of the temperature fluctuation. The Nusselt number distributions obtained for the flow cases with jet were then compared with the distributions obtained along the heated rotating disk in rotor/stator configurations, and also with the results obtained from the experimental correlation formula proposed by Nikitenko for the heated rotor. For all considered Reynolds numbers we observed two peaks of the Nusselt numbers near the impingement area and linear increase of Nusselt numbers outside this area. This preliminary research showed that investigations of the interaction between the axial annular jet and the heated rotating disk in the rotating cavity can deliver results interesting from fundamental and engineering points of view. Further research is planned on this problem to deliver more information about the influence of the geometrical parameters of the cavity ($H/a, L, Rm$) on the effectiveness of the heat transfer and on the near-rotating disk characteristics.

Our further research will also include the optimization of the numerical algorithm. We believe that the implementation of the multi-domain method together

with the MPI parallelization will allow us to perform computations in a shorter wall time and also will allow us to use better meshes.

Acknowledgement

We are grateful to the Poznań Supercomputing and Networking Center, where the computations have been performed and to authors of ParaView open source tool.

References

1. A. RANDRIAMAMPINANINA, L. ELENA, J.P. FONTAINE, R. SCHIESTEL, *Numerical prediction of laminar, transitional and turbulent flows in shrouded rotor-stator systems*, Phys. Fluids, **9**, 1696, 1997.
2. E. SERRE, J.P. PULICANI, *A three-dimensional pseudospectral method for rotating flows in a cylinder*, Computers & Fluids, **30**, 491, 2001.
3. E. SERRE, E. TULISZKA-SZNITKO, P. BONTOUX, *Coupled theoretical and numerical study of the flow transition between a rotating and a stationary disk*, Phys. Fluids, **16**, 3, 688–707, 2004.
4. M. LYGREN, H.I. ANDERSSON, *Large eddy simulations of the turbulent flow between a rotating and a stationary disk*, ZAMP, **55**, 268, 2004.
5. S. PONCET, R. SCHIESTEL, *Numerical modeling of heat transfer and fluid flow in rotor stator cavities with throughflow*, Int. J. Heat Mass Transfer, **50**, 1528–1544, 2007.
6. E. SEVERAC, E. SERRE, *A spectral vanishing viscosity for the LES of turbulent flows within rotating cavities*, J. Comput. Phys., **226**, 1234–1255, 2007.
7. A. RANDRIAMAMPINANINA, P. BONTOUX, B. ROUX, *Buoyancy driven flows in rotating cylindrical annulus*, Int. J. Heat Mass. Transfer, **30**, 1275–1292, 1987 [in French].
8. J. PELLE, S. HARMAND, *Heat transfer measurements in an opened rotor–stator system air gap*, Exp. Therm. Fluid Sci., **31**, 165–180, 2007.
9. E. TULISZKA-SZNITKO, W. MAJCHROWSKI, K. KIELCZEWSKI, *Investigation of transitional and turbulent heat and momentum transport in rotating cavity*, Int. J. Heat and Fluid Flow, **35**, 52–60, 2012.
10. E. TULISZKA-SZNITKO, A. ZIELINSKI, W. MAJCHROWSKI, *Large eddy Simulation of transitional flows in rotor/stator cavity*, Archives Mech., **61**, 2, 93–118, 2009.
11. C.J. ELKINS, J.K. EATON, *Turbulent heat and momentum transport on a rotating disk*, J. Fluid Mech., **402**, 225–253, 2000.
12. N. KASAGI, *Micro gas turbine/solid oxide fuel cell hybrid cycles for distributed energy system*, The University of Tokyo, 1999–2003.
13. H. WU, N. KASAGI, *Effects of arbitrary directional system rotation on turbulent channel flow*, Phys. Fluids, **16**, 979–990, 2004.
14. H. WU, N. KASAGI, *Turbulent heat transfer in a channel flow with arbitrary directional system rotation*, Int. J. Heat Mass Transfer, **47**, 4579–4591, 2004.

14. H. WU, N. KASAGI, *Turbulent heat transfer in a channel flow with arbitrary directional system rotation*, Int. J. Heat Mass Transfer, **47**, 4579–4591, 2004.
15. R. PASQUETTI, C.J. XU, *High-order algorithm for large eddy simulation of incompressible flow*, J. Sci. Comput., **17**, 1–4, 273, 2002.
16. E. SEVERAC, P. PONCET, E. SERRE, *A spectral vanishing viscosity for the LES of turbulent flows within rotating cavity*, J. of Comput. Physics, **226**, 1234–1255, 2007.
17. E. TADMOR, *Convergence of spectral methods for nonlinear conservation laws*, SIAM, J. Numer. Anal., **26**, 30–44, 1989.
18. G.S. KARAMANOS, G.E. KARNIADAKIS, *A spectral vanishing viscosity method for large eddy simulation*, J. Comput. Physics, **163**, 22, 2000.
19. Y. MADAY, S. KABER, E. TADMOR, *Legendre pseudo-spectral viscosity method for nonlinear conservation laws*, SIAM, J. Numer. Anal., **30**, 2, 321, 1993.
20. S. SARRA, CHEBYSHEV, *Pseudospectral methods for conservation laws with source terms and application to multiphase flow*, Phd Thesis, Morgantown, West Virginia, 2002.
21. K. HANJALIC, B. LAUNDER, *Modelling Turbulence in Engineering and the Environment*, Cambridge, 2011.
22. H. LITTELL, J. EATON, *An experimental investigation of the three-dimensional boundary layer on a rotating disk*, Tech. Rep. MD-60. Stanford University, Department of Mechanical, Engineering, Thermosciences Div., 1991.
23. J.M. OWEN, R.H. ROGERS, *Flow and heat transfer in rotating-disc systems, Part II*, Research Studies Press Taunton, Somerset, England.
24. E. CRESPO DEL ARCO, P. MAUBERT, A. RANDRIAMAMPINANINA, P. BONToux, *Spatio-temporal behaviour in a rotating annulus with a source-sink flow*, J. Fluid Mech., 328, 1996.
25. N. NIKITENKO, *Experimental investigation of heat exchange of a disk and screen*, J. Engng. Phys., **6**, 1–11, 1963.

Received January 29, 2013; revised version September 30, 2013.
